remote sensing

MDPI

Article

Recent Trends in Atmospheric Methane Growth Rates over Korea Revealed by Long-Term In-Situ Observations, Satellite and Transport Modeling

Samuel Takele Kenea *, Daegeun Shin, Wonick Seo, Sunran Lee, Sumin Kim and Sangbaek Kim

Global Atmosphere Watch and Research Division, National Institute of Meteorological Sciences (NIMS), 33, Seohobuk-ro, Seogwipo-si 63568, Jeju-do, Republic of Korea
* Correspondence: samueltake@korea.kr

Highlights

What are the main findings?

- Atmospheric CH_4 growth over Korea accelerated during 2020–2022 and decelerated markedly after 2021, consistent with East Asian and global XCH_4.
- STILT–EDGAR2025 sensitivity analysis showed that CH_4 enhancement variability at AMY was more sensitive to transport variability than to changes in prescribed emissions.

What are the implications of the main findings?

- Transport variability can strongly modulate observed CH_4 enhancements, highlighting the need to account for source–receptor transport when interpreting regional CH_4 variability and assessing emissions.
- Combining long-term multi-site observations with satellite and inventory constraints provides complementary information for characterizing CH_4 variability and improving emission assessment.

Abstract

Atmospheric methane (CH_4) growth accelerated strongly during 2020–2022 but subsequently decelerated, while the processes driving this transition remain poorly constrained over East Asia. We investigate CH_4 growth-rate variability over the Korean Peninsula during 2020–2025 using observations from three Global Atmosphere Watch stations—Anmyeondo (AMY), Jeju Gosan (GSN), and Ulleungdo (ULD)—combined with GOSAT (Greenhouse Gases Observing Satellite) XCH_4 observations, emission inventories, and climate indices. The longer 2009–2025 records provide historical context for recent changes. Atmospheric methane growth accelerated markedly during 2020–2022, although the timing of the peak differed among stations, and subsequently decelerated. Seasonal variability also intensified at AMY, with the seasonal amplitude increasing from 67.1 ppb in 2022 to 119.2 ppb in 2025, reflecting changes in both rising seasonal maxima and declining summer minima. During 2021–2025, CH_4 growth rates declined significantly in global XCH_4 (-3.13 ppb yr^{-2}, $p = 0.002$), East Asian XCH_4 (-2.04 ppb yr^{-2}, $p = 0.004$), and GSN (-3.7 ppb yr^{-2}, $p = 0.04$). EDGAR2025 indicates weakening tendencies in year-to-year emission growth across China and Korea, although changes in total regional emissions were not statistically significant. STILT (Stochastic Time-Inverted Lagrangian Transport)–EDGAR2025 counterfactual sensitivity analysis at AMY further indicates that transport variability exerted a stronger influence on interannual modeled CH_4 enhancement than changes in prescribed emissions: relative to the 2018 reference, the 2021 enhancement showed an 18.4 ppb transport sensitivity compared with 3.4 ppb emission sensitivity. After 2021, transport continued to show greater sensitivity than changes in prescribed emissions, while the emission-related

Check for updates

Academic Editor: Ge Han

Received: 7 October 2026
Revised: 13 November 2026
Accepted: 23 November 2026
Published: 25 November 2026

Copyright: © 2026 by the authors. Licensee MDPI, Basel, Switzerland. This article is an open access article distributed under the terms and conditions of the Creative Commons Attribution (CC BY) license.

sensitivity decreased from 2.4 ppb in 2022 to 1.0 ppb in 2023 and 0.7 ppb in 2024. These results suggest that weakening regional emission growth was associated with the post-2021 slowdown, while atmospheric transport variability substantially modulated modelled CH_4 enhancements at AMY. The concurrent regional and global deceleration also points a broader atmospheric processes. These findings demonstrate the value of long-term multi-site observations combined with satellite, inventory, and transport constraints characterizing regional source and transport influences on atmospheric CH_4 variability over East Asia.

Keywords: methane growth rate; East Asia; XCH_4; STILT; EDGAR emission

1. Introduction

Methane (CH_4) is the second-largest contributor to anthropogenic greenhouse-gas forcing after carbon dioxide (CO_2) and is a critical target for near-term climate mitigation, owing to its strong radiative efficiency and short atmospheric lifetime of approximately a decade [1]. Updated radiative-transfer calculations indicate that methane's forcing is substantially larger than previously estimated, partly due to its shortwave absorption [2], and its short lifetime means that CH_4 mitigation can deliver climate benefits far more rapidly than CO_2 reduction alone [3,4]. This urgency motivated the Global Methane Pledge (https://www.globalmethanepledge.org/news/factsheet-2024-global-methane-pledge-ministerial, accessed on 3 August 2026), launched in 2021 with a collective goal of reducing anthropogenic CH_4 emissions by at least 30% from 2020 levels by 2030; the Republic of Korea joined the Pledge and incorporated the 30% target into its national climate strategy [5].

Despite this mitigation ambition, atmospheric CH_4 has continued to increase. After a temporary slowdown in the early 2000s, growth resumed after 2007 and accelerated markedly during the late 2010s and early 2020s, reaching unprecedented levels in 2020–2022 [6,7]. This acceleration cannot be attributed to a single cause: because atmospheric growth reflects the balance between heterogeneous emissions and OH-driven removal, recent global analyses attribute the 2020–2021 surge to a combination of enhanced natural emissions—particularly from wetlands—a weakened OH sink, and continued growth in several anthropogenic sectors [7,8]. More recently, growth decelerated substantially during 2023–2024 even as global emissions remained elevated, and this deceleration has itself been linked to a partial recovery of the atmospheric OH sink [9], underscoring that sink variability, not emissions alone, exerts first-order control on year-to-year CH_4 growth.

The extent to which these global processes explain regional atmospheric CH_4 variability remains poorly constrained. East Asia hosts major agricultural, waste, fossil-fuel, and industrial CH_4 sources, and its monsoon circulation and strong seasonality provide an additional pathway through which climate can modulate both emissions and atmospheric transport: interannual temperature and precipitation anomalies affect wetland and agricultural emissions, while large-scale circulation governs the relative influence of different continental source regions on individual receptor sites. TROPOMI and GOSAT observations have substantially improved the ability to resolve these regional patterns and have been used to quantify CH_4 emissions from China and other major East Asian source regions [10–12]. Here, we complement these satellite-based constraints with long-term, high-precision in-situ observations, which provide the temporal continuity needed to track year-to-year changes in atmospheric CH_4 growth rate at fixed receptor locations.

The operational in-situ network over South Korea, located downwind of major East Asian source regions, provides a valuable setting for investigating regional CH_4 variability. The Korea Meteorological Administration (KMA) has maintained continuous CH_4 observa-

tions at Anmyeondo (AMY) since 1999 and subsequently expanded the network to Jeju Gosan (GSN) and Ulleungdo (ULD), providing complementary sensitivity to continental and maritime air masses [13]. Long-term observations have documented persistent increases in atmospheric CH_4 and substantial interannual variability, with the AMY growth rate increasing from approximately 3.3 ppb yr^{-1} during 2006–2010 to 8.3 ppb yr^{-1} during 2016–2020 [13]. Source and isotopic studies further demonstrate that Korean CH_4 variability reflects contributions from transboundary transport, biogenic and fossil-fuel sources, and climate-sensitive processes [13–15]. In particular, Kenea et al. [14] showed contrasting drivers of the 2015–2016 and 2019 CH_4 growth episodes, with the former associated with strong El Niño conditions and the latter characterized by isotopic evidence of enhanced biogenic emissions. Recent top-down inversion studies using the Korean network have further provided constraints on domestic CH_4 emissions [16]. However, the recent evolution of CH_4 growth rates during the pronounced changes in atmospheric methane since 2020, particularly the post-2021 deceleration, has not been systematically evaluated across the Korean network together with spatially resolved satellite XCH_4 observations. A key unresolved question, therefore, is whether the major features of the recent global methane record—the 2020–2022 acceleration and its subsequent deceleration—are expressed consistently over the Korean Peninsula, and which processes control their regional expression. Growth rate is particularly informative in this context because it integrates simultaneous changes in emissions and removal and can reveal rapid shifts that are less apparent in the absolute concentration record. Comparing growth rates among AMY, GSN, and ULD, alongside satellite-derived XCH_4 over Korea and East Asia, makes it possible to distinguish coherent large-scale signals from site-specific variability driven by transport and source distribution.

Here, we investigate the interannual and seasonal variability of atmospheric CH_4 growth over the Korean Peninsula using long-term observations from AMY, GSN, and ULD, together with satellite-derived XCH_4 over Korea, East Asia, and the global domain. We first characterize the long-term evolution and seasonal structure of CH_4 and quantify the timing and magnitude of major growth-rate episodes. We then examine the pronounced acceleration during the late 2010s and early 2020s and the subsequent decline in growth during 2021–2025, evaluating how these changes relate to year-to-year variations in regional sectoral CH_4 emissions, environmental conditions, large-scale climate variability, and biomass-burning influence. By integrating surface observations, satellite XCH_4, emission inventories, meteorological information, and receptor-scale transport–emission sensitivity analysis, this study provides a regional perspective on how the recent methane perturbation has manifested over East Asia and identifies the roles of regional emissions and atmospheric transport variability in shaping the observed CH_4 signal. These results provide observational constraints relevant to improving inverse-modeling frameworks for quantifying Korean and East Asian methane emissions.

2. Data and Methods

2.1. Near-Surface In-Situ CH_4 Observations

Atmospheric CH_4 measurements were obtained from three stations operated by the Korea Meteorological Administration (KMA) as part of the World Meteorological Organization Global Atmosphere Watch (WMO/GAW) programme (Figure 1). KMA has conducted continuous CH_4 monitoring at Anmyeondo (AMY; 36.54°N, 126.33°E; 47 m above sea level (a.s.l.)) since 1999. The AMY sampling inlet was located at 20 m above ground level during 1999–2004 and has been located at 40 m since 2004. Observations were subsequently expanded to Gosan, Jeju (GSN; 33.29°N, 126.16°E; 71.47 m a.s.l.; inlet height 12 m) and Ulleungdo (ULD; 37.48°N, 130.90°E; 220.9 m a.s.l.; inlet height 10 m), both beginning in 2012. Although measurements at GSN and ULD began in 2012, the continuous records

used in the present analysis cover 2014–2025 and 2015–2025, respectively. The stations are equipped with cavity ring-down spectroscopy (CRDS) analyzers (Picarro, Inc., Santa Clara, CA, USA) for continuous, high-precision CH_4 measurements. At AMY, CRDS measurements have been available since 2016, while measurements before 2016 were obtained using gas chromatography with flame ionization detection (GC-FID). Prior to February 2016, measurements were made at 30-min intervals using GC-FID and calibrated against KRISS standards, which agreed with the WMO-X2004A scale within −0.1 to 0.8 ppb. WMO Round Robin 5 comparisons showed offsets of −0.3 to 1.3 ppb relative to the WMO Central Calibration Laboratory (CCL). In February 2016, AMY transitioned to continuous CRDS (Picarro) measurements at 5-s intervals using WMO-traceable standards, with reported measurement uncertainties of approximately ±0.7–0.8 ppb (68% confidence interval) [13]. Although differences between GC-FID and CRDS are recognized, the primary analysis focuses on 2021–2025, entirely within the CRDS measurement period. All observations were processed following WMO/GAW quality-assurance procedures and are reported on the WMO CH_4 calibration scale (WMO-X2004A). For this study, we used Level 3 (L3) data, which provide regional background CH_4 mole fractions for each station. Detailed descriptions of the CH_4 measurement procedures, quality control, and regional-background selection are provided in [13]. The three stations provide complementary sampling of continental and marine air masses across and around the Korean Peninsula [13,16,17].

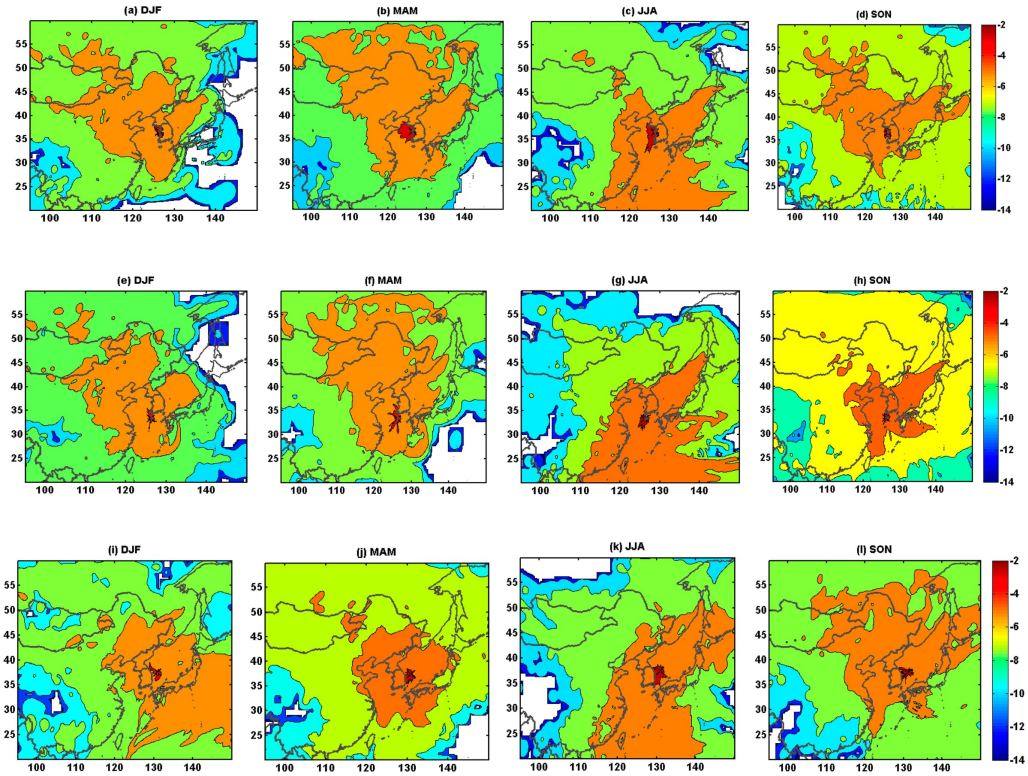

Figure 1. Seasonal footprint sensitivity distributions derived from STILT for the AMY, GSN, and ULD in 2020. Colors indicate the sensitivity of each receptor to surface fluxes in the upwind region. Each station is indicated by marker 'x'. The unit of footprint is $\log_{10}(\text{ppm}/\mu\text{mol m}^{-2}\ \text{s}^{-1})$.

AMY, located on the western coast of the Korean Peninsula, is exposed to both regional anthropogenic emissions and long-range transport from continental East Asia. Its surrounding region includes extensive agricultural activities, particularly rice cultivation and livestock production, as well as industrial and power-generation facilities. These nearby and regional sources can influence the observed CH_4 variability, particularly when air masses pass over the Korean Peninsula and adjacent continental source regions. Changes in

wind direction and regional circulation can modify the relative influence of local, regional, and more distant sources. Consequently, AMY is particularly sensitive to variations in continental air-mass influence and regional source activity, which may contribute to its relatively pronounced atmospheric CH_4 variability [13]. GSN, located on the western coast of Jeju Island, provides observations under a combination of maritime and continental atmospheric influences. Its geographical position exposes the station to air masses transported across the Yellow Sea and East China Sea, as well as continental outflow from eastern China and the Korean Peninsula. The relative influence of these air masses varies with prevailing synoptic circulation and seasonal monsoon patterns. Although maritime air masses generally provide relatively clean background conditions, continental transport can episodically enhance atmospheric CH_4 at the station. Previous investigations at Gosan have demonstrated the alternating influence of relatively clean maritime air and polluted continental outflow, highlighting the importance of air-mass origin in interpreting atmospheric composition [16,17]. Thus, GSN represents an important receptor for examining the interaction between regional continental outflow and marine atmospheric transport. ULD, situated on Ulleungdo Island in the East Sea, represents a more maritime observational environment, relatively distant from major continental emission regions. Its island setting and surrounding ocean generally favor the sampling of marine air masses, resulting in a weaker direct influence from nearby continental anthropogenic sources than at AMY. Nevertheless, the station is not completely isolated from regional emissions. Depending on synoptic circulation and wind direction, air masses transported from the southeastern Korean Peninsula and other continental source regions can episodically influence its observations. These characteristics make ULD valuable for examining methane variability under predominantly maritime conditions and for identifying regional atmospheric influences that extend beyond the immediate Korean mainland [13,16,17].

Growth Rate and Seasonal Amplitude Analysis

To characterize interannual CH_4 variability while accounting for the strong seasonal cycle, monthly year-on-year CH_4 growth rates were calculated as the difference between monthly mean mole fractions for the same calendar month:

$$G_{m,y} = C_{m,y} - C_{m,y-1} \quad (1)$$

where $G_{m,y}$ is the CH_4 growth rate for month m in year y, $C_{m,y}$ is the monthly mean CH_4 mole fraction for month m in year y, and $C_{m,y-1}$ is the monthly mean CH_4 mole fraction for the corresponding month in the previous year. For annual growth rates, the difference between the annual mean CH_4 mole fraction in year y and that in the preceding year was calculated. To account for temporal dependence in monthly CH_4 growth-rate observations, we evaluated their linear trends using generalized least-squares (GLS) regression with autoregressive moving-average (ARMA) error structures. Unlike ordinary least-squares (OLS) regression, GLS allows the residuals to exhibit temporal correlation, thereby providing more appropriate estimates of parameter uncertainty when observations are serially dependent [18,19]. Model adequacy was evaluated by examining the autocorrelation and partial autocorrelation functions (ACF and PACF) of the residuals and applying the Ljung–Box tests at lags 12 and 24 to assess remaining temporal autocorrelation [20]. Residual heteroscedasticity was evaluated using the Breusch–Pagan test, while the presence of autoregressive conditional heteroscedasticity was examined using ARCH diagnostics [21,22]. GLS estimates, corresponding 95% confidence intervals, and p-values were used to evaluate the direction and statistical significance of the growth-rate trends.

To evaluate the recent changes in atmospheric methane growth rates in the context of their long-term variability, breakpoint analysis was conducted using the complete available

historical records. Continuous piecewise-linear regression with an unknown breakpoint was applied to identify potential changes in growth-rate trends. The optimal breakpoint was determined using the Bayesian Information Criterion (BIC), and its statistical significance was evaluated using the Monte Carlo sup-F and Davies tests. Bootstrap analysis was used to assess breakpoint uncertainty, while leave-one-year-out and alternative minimum-segment-length tests were conducted to examine the robustness of the estimated breakpoint. The uncertainty of the annual CH_4 growth-rate estimates was evaluated by considering measurement uncertainty and sampling/data-completeness uncertainty. Measurement uncertainties of approximately 0.73–0.80 ppb for the three Korean GAW stations were adopted from Lee et al. [13]. Sampling and data-completeness uncertainty was estimated using a bootstrap resampling approach (N = 10,000) applied to the available daily observations within each month, accounting for synoptic temporal variability. These uncertainty components were propagated to the yearly CH_4 growth-rate estimates, yielding a total uncertainty of 1.15 ppb.

To characterize changes in the seasonal cycle of atmospheric CH_4 at the AMY site, seasonal amplitude was evaluated using three complementary approaches: (1) the monthly maximum-minus-minimum method, (2) first-order harmonic regression, and (3) Seasonal-Trend decomposition using LOESS (STL). Monthly mean CH_4 mole fractions were used for all analyses to ensure consistency in temporal resolution. Initially, the conventional seasonal amplitude was calculated for each calendar year as the difference between the highest and lowest monthly mean CH_4 mole fractions:

$$A_{range,y} = \max(CH_4, y, m) - \min(CH_4, y, m) \quad (2)$$

where y and m denote the year and month, respectively. Although this approach provides a straightforward measure of the observed annual concentration range, it can be sensitive to individual monthly values and anomalous observations. Therefore, harmonic regression and STL decomposition were additionally applied to obtain complementary estimates of seasonal variability. For harmonic regression, the monthly mean CH_4 observations were fitted using a first-order annual harmonic model:

$$CH_4(m) = \beta_o + asin\left(\frac{2\pi m}{12}\right) + bcos\left(\frac{2\pi m}{12}\right) + \epsilon_m \quad (3)$$

where β_o represents the mean concentration level, a and b are the fitted harmonic coefficients, and ϵ_m represents the residual error. The annual peak-to-trough seasonal amplitude (A) was calculated as: $A = 2\sqrt{a^2 + b^2}$.

The corresponding seasonal maximum (S_{max}) and minimum (S_{min}) deviations from the fitted mean were calculated as: $S_{max} = \sqrt{a^2 + b^2}$ and $S_{min} = -\sqrt{a^2 + b^2}$.

This approach estimates the amplitude of the fitted annual cycle using all monthly observations rather than depending exclusively on the two most extreme monthly values. As an independent decomposition approach, STL was applied to separate the observed CH_4 time series into long-term trend, seasonal, and residual components:

$$CH_4(t) = T(t) + S(t) + R(t), \quad (4)$$

where T(t), S(t), and R(t) represent the trend, seasonal, and residual components, respectively. The annual seasonal amplitude was calculated from the peak-to-trough range of the extracted seasonal component within each calendar year: $A_{STL,y} = \max(S_y) - \min(S_y)$.

Comparing harmonic regression and STL estimates provides an assessment of the sensitivity of the inferred seasonal amplitude to the method used to characterize the annual cycle. Uncertainty in the annual amplitude estimates and their seasonal maxima and minima was evaluated using bootstrap resampling. For each bootstrap replicate, the corresponding seasonal model was refitted and the amplitude and seasonal extrema were recalculated.

The 2.5th and 97.5th percentiles of the resulting bootstrap distributions were used to derive 95% confidence intervals. Normalized monthly deviation was calculated from its deviation from the mean monthly CH_4 growth rate within each year. For year y and month m, the monthly deviation ($D_{y,m}$) was $D_{y,m} = g_{y,m} - \overline{g}_y$ where $g_{y,m}$ is the monthly year-on-year CH_4 growth rate and $\overline{g}_y$ is the annual mean of the 12 monthly growth rates. The normalized monthly deviation ($RI_{y,m}$ in %) was then calculated as $RI_{y,m} = 100 \times D_{y,m} / \sum_{m=1}^{12} |D_{y,m}|$. The normalized monthly deviation indicates whether the monthly CH_4 growth rate was higher or lower than the annual mean and quantifies the magnitude of its departure from that mean. It was used as a diagnostic measure of seasonal variability and does not represent a quantitative contribution of an individual month to the annual CH_4 growth rate.

2.2. STILT Model

The Stochastic Time-Inverted Lagrangian Transport (STILT) model version 2 [23] was used to characterize atmospheric transport pathways and upwind source regions influencing the Korean CH_4 observation sites. STILT is a receptor-oriented Lagrangian particle dispersion model that traces ensembles of air parcels backward from a receptor location to quantify the spatial influence of upstream surface sources [23,24]. Meteorological forcing was provided by the ERA5 reanalysis, which provides hourly meteorological fields for simulating atmospheric transport [25]. For each observation, 500 particles were released hourly from the receptor at the corresponding inlet height: 40 m above ground level (a.g.l.) at AMY, 12 m at GSN, and 10 m at ULD. The particles were tracked backward for 5 days, and the resulting particle distributions were used to derive surface influence footprints on a 0.1° × 0.1° horizontal grid covering East Asia. Seasonal footprints were averaged for December–February (DJF), March–May (MAM), June–August (JJA), and September–November (SON) to characterize seasonal changes in dominant upwind source regions and transport pathways. These footprints provide a transport-based framework for interpreting seasonal and interannual variability in CH_4 observed at the Korean stations. Figure 1 presents representative seasonal-mean STILT footprints for AMY, GSN, and ULD for 2020. All three stations exhibit pronounced seasonal differences in transport regimes. During DJF–MAM, the footprints show broader continental influence, associated primarily with northwesterly transport from eastern China and the Korean Peninsula. In contrast, during JJA, southerly and maritime flow generally restricts continental influence and shifts the dominant source regions toward the Korean Peninsula and surrounding marine areas. SON represents a transitional transport regime between the winter–spring and summer patterns.

To investigate the role of interannual variability in CH_4 growth rates observed at AMY, we further combined STILT footprints with the EDGAR2025 CH_4 emission inventory in a receptor-scale counterfactual framework. This approach was used to quantify the relative sensitivity of modeled CH_4 enhancements to variations in atmospheric transport and regional emissions. The modeled CH_4 enhancement (ΔCH_4) at the receptor was calculated as

$$\Delta CH_4 = \sum_{i=1}^{n} F_i E_i \quad (5)$$

where F_i represents the STILT footprint or surface influence at grid cell i, E_i represents the corresponding CH_4 emission flux from EDGAR2025, and n is the total number of grid cells within the modeling domain. A two-factor, two-level factorial design was implemented, with atmospheric transport and CH_4 emissions independently represented by a reference condition (2018) and a year-specific condition y. Four simulations were therefore considered: (1) reference transport with reference emissions C_{00}; (2) year-specific transport with reference emissions C_{10}; (3) reference transport with year-specific emissions C_{01}; and (4) year-specific transport with year-specific emissions C_{11}. The 2018 reference

year was selected to represent a pre-COVID-19 atmospheric and emission condition. The transport effect S_T and emission effect S_E were calculated by comparing each individual factor against the reference simulation, while their interaction I_{TE} was quantified using the difference-in-differences approach:

$$I_{TE}(y) = C_{11}(y) - C_{10}(y) - C_{01}(y) + C_{00} \quad (6)$$

$$S_T(y) = C_{10}(y) - C_{00} \quad (7)$$

$$S_E(y) = C_{10}(y) - C_{00} \quad (8)$$

The total modeled enhancement difference was then decomposed into the transport effect, emission effect, and their interaction:

$$\Delta C_{Total}(y) = S_T(y) + S_E(y) + I_{TE}(y) \quad (9)$$

The calculations were performed for each analysis year using consistent temporal sampling and spatial aggregation. This framework was applied to AMY to investigate the relative sensitivity of modeled receptor-level CH_4 enhancements to interannual changes in atmospheric transport and emissions. In short, three counterfactual experiments were considered: (1) actual transport with actual-year emissions, (2) variable transport with emissions fixed to 2018 baseline, and (3) transport fixed to the 2018 baseline with variable-year emissions. Differences among these experiments were used to evaluate the relative sensitivity of the modeled receptor-scale CH_4 enhancement to atmospheric transport and prescribed emission variability. The resulting STILT–EDGAR enhancement represents the transport-weighted influence of prescribed regional surface emissions and is not intended to reconstruct the absolute observed CH_4 concentration or a complete regional source–sink budget. STILT provides receptor sensitivity to upstream surface fluxes, whereas background and boundary CH_4 variability and atmospheric removal by OH were not explicitly resolved in this calculation. Given the multi-year atmospheric lifetime of CH_4, chemical loss over the 5-day transport window is expected to be relatively small compared with transport and dilution effects; nevertheless, temporal and regional variability in OH remains an unresolved source of uncertainty. The modeled enhancement is also subject to uncertainties in atmospheric transport and the prescribed EDGAR2025 emissions. Therefore, the counterfactual experiments are interpreted as sensitivity analyses rather than as a quantitative partition of the observed CH_4 variability.

2.3. Satellite Observations of Column-Averaged CH_4 (XCH_4)

Satellite observations were used to provide independent information on the spatial distribution and temporal evolution of atmospheric methane over East Asia. Satellite-derived column-averaged dry-air CH_4 mole fractions (XCH_4) complement the high-precision but spatially limited surface observations by providing spatially continuous information over regional and continental scales.

2.3.1. GOSAT XCH_4 Observations

GOSAT-derived XCH_4 observations were used to characterize the long-term evolution of column-averaged atmospheric CH_4 (XCH_4) over the Korean Peninsula, East Asia, and the global domain. GOSAT/GOSAT-2 Level 2 (L2) XCH4 retrievals (version v02.96 and v02.10) were used in this study. Monthly mean XCH_4 values were calculated for the AMY region, South Korea, East Asia, and the global domain. These spatial averages were used to examine the consistency of the temporal evolution of satellite-derived XCH_4 with near-surface CH_4 observations at the Korean monitoring stations. Monthly GOSAT XCH_4 growth rates were calculated using the same year-to-year difference applied to the

surface observations. GOSAT XCH_4 retrievals are based on measurements from the TANSO-FTS shortwave-infrared bands and have been extensively validated against ground-based observations [26–28]. Near-surface in-situ CH_4 and satellite-derived XCH_4 represent different atmospheric quantities with distinct vertical sensitivities. Since satellite averaging kernels and a priori CH_4 profiles were not explicitly applied to the surface observations, their comparison is intended to assess temporal and regional consistency rather than quantitative agreement in absolute mole fractions. Differences may arise from vertical sensitivity, satellite sampling, cloud screening, and spatial representativeness. Accordingly, their consistency is interpreted as evidence of coherent temporal variability across different atmospheric sampling scales, rather than direct quantitative validation or equivalence between the two measurements.

2.3.2. Sentinel-5P/TROPOMI XCH_4 Observations

Spatial and interannual variations in atmospheric XCH_4 over Korea and East Asia were examined using Sentinel-5P/TROPOMI Level-3 (L3) gridded products derived Level-3 (L3) gridded products derived from Sentinel 5 collection 3 CH_4 L2 retrievals. TROPOMI provides high-density observations of column-averaged dry-air CH_4 (XCH_4) with broad spatial coverage, enabling characterization of regional spatial patterns and year-to-year changes that are not resolved by surface observations alone. The operational XCH_4 product is retrieved using the RemoTeC algorithm, which accounts for atmospheric scattering and aerosol effects [29]. Quality-filtered L3 products were obtained from the Sentinel-5P Product Algorithm Laboratory (S5P-PAL) data portal (https://browser.moregeo.it/external/data-portal.s5p-pal.com/api/s5p-l3/ch4/, accessed on 10 July 2026). The S5P-PAL CH4 product applies a quality-assurance filter of qa_value > 0.5 prior to gridding. Gridded yearly-mean L3 XCH_4 products were used directly, and differences between consecutive years were calculated to characterize year-to-year spatial changes in XCH_4 over Korea and East Asia. The quality-filtered TROPOMI CH_4 product has been extensively evaluated against independent ground-based observations, including TCCON and NDACC measurements [30,31].

2.4. CH_4 Emission Datasets

Anthropogenic CH_4 emissions were obtained from the EDGAR 2025 (version 9) Community GHG Database developed by the European Commission Joint Research Centre (JRC) [32,33]. The dataset provides annual country-level and $0.1° \times 0.1°$ gridded CH_4 emissions by sector, agriculture (including rice cultivation, enteric fermentation, and manure management), fossil fuel exploitation (coal, oil, and natural gas), and waste management (solid waste disposal and wastewater treatment), 1970 through 2024. We used EDGAR 2025 to quantify total and sector-specific CH_4 emissions for major East Asian countries and to calculate year-to-year emission changes (ΔE) during 2020–2024. It is noted that EDGAR-based results are interpreted as anthropogenic emission tendencies rather than estimates of total natural and anthropogenic methane emissions. Although atmospheric observations extend through 2025, the available EDGAR2025 inventory does not include 2025 emission estimates. Therefore, the inventory-based analyses are restricted to the available years, and the 2025 atmospheric observation are not directly attributed to EDGAR-derived emissions. Biomass-burning CH_4 emissions were obtained from the Global Fire Emissions Database version 5 (GFED5) [34], which provides satellite-constrained fire emissions based on burned area, fuel characteristics, combustion, and emission factors. We used GFED5 CH_4 emissions to calculate fire-emission anomalies and assess their relationship with interannual CH_4 growth-rate variability over Korea. Together, EDGAR and GFED5 provide complementary information on anthropogenic and fire-related CH_4 sources, respectively, allowing source-side variability to be evaluated alongside the atmospheric observations.

2.5. Climatic Indices

The Oceanic Niño Index (ONI), obtained from the NOAA Climate Prediction Center (https://psl.noaa.gov/data/, accessed on 1 June 2026), was used to examine the relationship between El Niño–Southern Oscillation (ENSO) [30] variability and interannual CH_4 growth. ENSO is a major mode of interannual climate variability that modulates temperature and precipitation across East Asia and other regions [35].

3. Results and Discussion

3.1. Long-Term Evolution and Seasonal Cycle of Atmospheric CH_4 over Korea

Figure 2's top panel presents monthly mean atmospheric CH_4 mole fractions at the three Korean GAW stations (AMY, GSN, and ULD) during 2009–2025. All sites show a persistent long-term increase superimposed on a pronounced seasonal cycle, with a characteristic minimum in July–August and a broad autumn-to-winter maximum, consistent with enhanced summertime OH-driven photochemical removal [36,37]. Short-term variability is largest at AMY, consistent with its greater exposure to continental outflow and regional sources, while GSN and ULD show smoother variations. The full-record mean seasonal amplitude was largest at GSN (~80–85 ppb), intermediate at AMY (~65 ppb), and smallest at ULD (~60 ppb), highlighting site-dependent differences in seasonal CH_4 variability and source–transport influence. AMY exhibited a pronounced increase in seasonal amplitude after 2022, from 67.1 ppb in 2022 to 85.8, 105.7, and 119.2 ppb in 2023–2025, respectively (Figure 2, bottom panel). The 2025 amplitude was nearly twice the full-record mean. This widening reflected both a rising seasonal maximum (2033.5 to 2063.6 ppb) and a declining minimum (1966.4 to 1944.5 ppb), with the initial increase dominated by the rising maximum and the later expansion increasingly reinforced by the lower summer minimum. Given the short four-year sequence, this increase is regarded as a recent observational feature rather than a statistically established trend or evidence for a specific mechanism. The widening seasonal contrast may reflect changes in regional source influence, air-mass origin, boundary-layer mixing, or atmospheric removal, including enhanced summertime OH [38]. The wider standard-deviation ranges during June–September indicate greater interannual variability in summer and provide context for the growth-rate changes discussed in Section 3.4.

3.2. Interannual Variability of CH_4 Growth

Examination of the complete historical records (2009–2025, depending on dataset availability) revealed substantial interannual variability in atmospheric methane growth rates. Particularly elevated growth was observed around 2020–2021, followed by generally weaker growth rates in subsequent years. Breakpoint analysis indicated a transition around 2021–2022, although its statistical support varied among datasets. The global XCH_4 record identified 2022 as the preferred breakpoint (ΔBIC = 10.9; sup-F $p = 0.0025$; Davies $p = 0.007$), whereas East Asian XCH_4 record identified 2021 (ΔBIC = 5.8; sup-F $p = 0.010$; Davies $p = 0.020$). Accordingly, 2021 is used as the starting point of the recent transition-focused analysis. Annual CH_4 growth rates derived from the Korean in-situ observations reveal substantial interannual variability superimposed on the long-term atmospheric increase (Figure 3). Despite differences in magnitude, AMY, GSN, and ULD show broadly coherent temporal evolution, with moderate growth during the early 2010s, weaker growth around 2017–2018, a pronounced increase during 2019–2021, and a subsequent decline after 2021. The common timing indicates that the dominant interannual variability extends beyond individual observation sites, although its amplitude is strongly site-dependent. AMY exhibits the largest year-to-year variability (−13 to +23 ppb yr^{-1}), consistent with its greater sensitivity to continental source regions and changing source–receptor transport

pathways, whereas GSN and ULD show comparatively smoother variations. The agreement with East Asian and global XCH_4 growth rates from GOSAT further demonstrates that the Korean observations capture regional-to-global CH_4 variability rather than solely local source fluctuations. It is noted that satellite averaging kernels and a priori CH_4 profiles were not explicitly applied to the near-surface in-situ observations. The comparison between the surface and satellite records was intended primarily to assess temporal and regional consistency in CH_4 variability, rather than quantitative agreement in absolute CH_4 mole fractions.

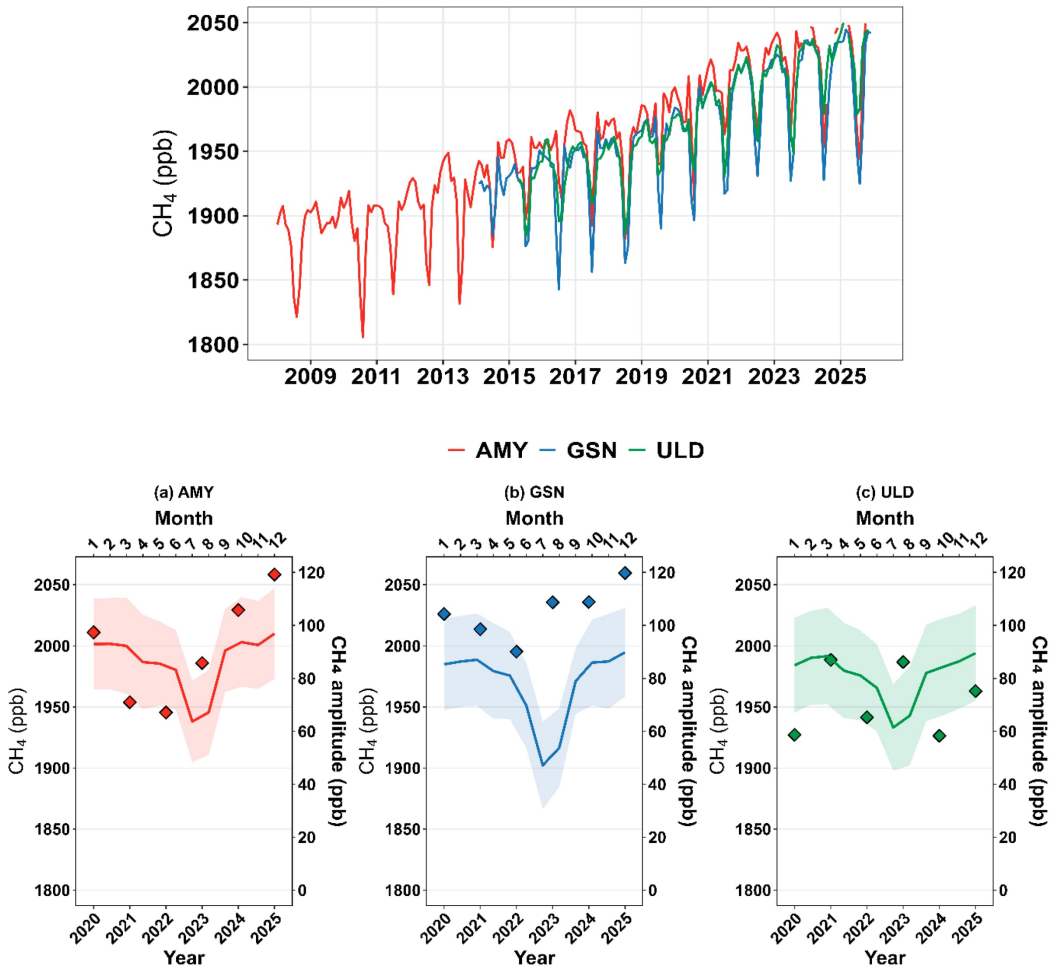

Figure 2. Time series of monthly mean atmospheric CH_4 mole fractions measured by near-surface in-situ at AMY, GSN, and ULD stations during 2009–2025. Bottom panels: Mean seasonal cycles during 2015–2025, shaded range represents standard deviation and diamond marker plots show the annual seasonal-cycle amplitude during 2020–2025, calculated as the difference between the seasonal maximum and minimum CH_4 mole fractions.

The normalized monthly deviations provide further evidence that the interannual variability in CH_4 growth is seasonally organized (Figure 4). Across all three stations, the largest positive and negative departures are concentrated during the summer months, particularly July–September, whereas winter and spring generally exhibit weaker and more spatially diffuse anomalies. This seasonal structure is most pronounced at AMY, where large positive and negative growth anomalies repeatedly occur during July–August, but a similar summer concentration is evident at GSN and ULD. The normalized monthly deviation analysis therefore indicates that summer months often exhibit relatively large departures from the annual mean growth level, although the magnitude and timing of these departures differ among stations. Thus, the interannual variability in annual CH_4 growth is

not evenly distributed throughout the year; rather, preferentially expressed during periods of the warm season when regional emissions, atmospheric transport, and atmospheric removal processes may undergo substantial changes. The stronger and more variable summer response at AMY is consistent with its greater exposure to continental source regions, while the comparatively smoother patterns at GSN and ULD suggest different source–receptor influences associated with their more maritime exposure. Overall, Figure 4 demonstrates that seasonal departures, particularly during summer, contribute substantially to the interannual variability in CH_4 growth, rather than the annual changes being expressed uniformly across all months.

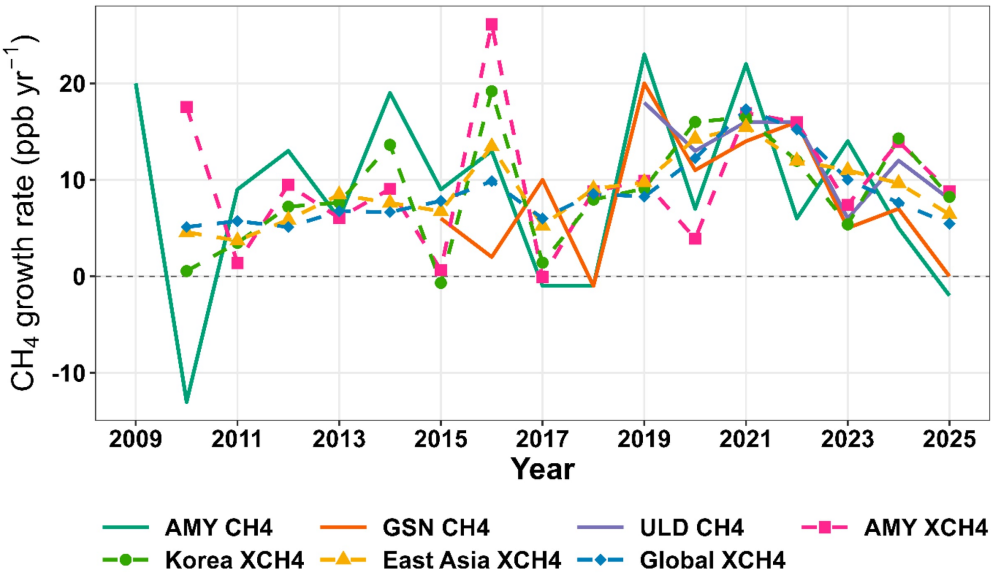

Figure 3. Annual atmospheric CH_4 growth rates derived from the Korean in-situ observations at AMY, GSN, and ULD, together with GOSAT satellite-derived XCH_4 growth rates over AMY, Korea, East Asia, and global.

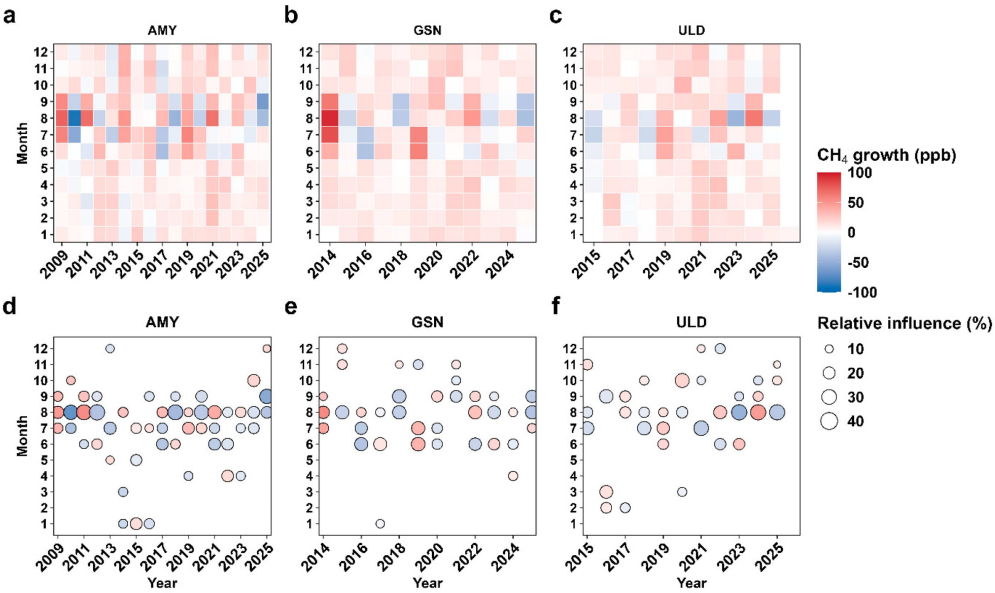

Figure 4. (**a**–**c**) Heatmaps show monthly CH_4 growth rates derived from in-situ observations at AMY, GSN, and ULD, respectively. (**d**–**f**) Bubble plots show the relative influence (%) of monthly CH_4 growth on the corresponding annual growth rate, with larger circles indicating greater relative influence.

The largest departures from the long-term trajectory occurred during 2019–2022, with the strongest and most spatially coherent enhancement during 2020–2022 (Figure 3). At GSN, CH_4 growth increased from ~11 ppb yr^{-1} in 2020 to 14 and 16 ppb yr^{-1} in 2021 and 2022, respectively, while ULD showed a comparable increase from ~13 to 16 ppb yr^{-1}. The simultaneous enhancement at these stations, despite their different atmospheric exposure, indicates that the episode was not confined to a single Korean source region but represented a broader regional-to-large-scale perturbation coincident with the global methane-growth surge [39]. Satellite observations provide independent spatial support, with TROPOMI XCH_4 difference maps showing coherent positive and negative anomalies across East Asia during several years (Figure 5). AMY exhibited a substantially larger and more transient response, with growth increasing from ~7 ppb yr^{-1} in 2020 to ~22 ppb yr^{-1} in 2021 before declining to ~6 ppb yr^{-1} in 2022. This contrast demonstrates that the common large-scale enhancement was strongly modulated by regional source–transport conditions. The greater sensitivity of AMY to continental outflow likely amplified the regional expression of the broader methane perturbation, whereas the more maritime exposure of GSN and ULD produced smoother responses. Previous observations support the importance of regional source heterogeneity, including depleted $\delta^{13}C$–CH_4 signatures during high-growth periods at AMY [14] and strong spatial CH_4 gradients over western Korea and eastern China from aircraft observations [40].

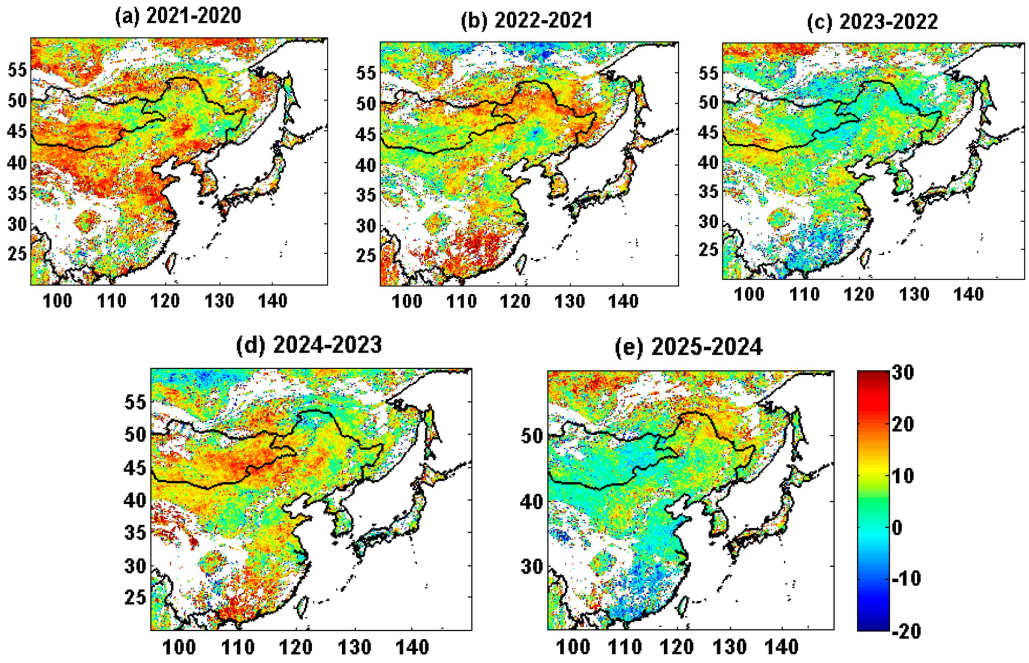

Figure 5. Spatial distributions of year-to-year differences in XCH_4 over East Asia during 2021–2025, derived from TROPOMI observations.

The Korean observations are consistent with the broader atmospheric methane enhancement reported globally and across East Asia during 2020–2021. In Japan, the Japan Meteorological Agency (JMA) reported substantial increases in surface CH_4 at three monitoring stations: Ryori (16 ppb), Minamitorishima (19 ppb), and Yonagunijima (13 ppb) between 2020 and 2021. These represented the largest annual increases at Ryori and Minamitorishima and the third largest at Yonagunijima since observations began [41]. At the global scale, Michel et al. [39] documented exceptionally high atmospheric CH_4 growth during 2020–2022 and identified enhanced microbial emissions as an important contributor. Together, these observations indicate that the pronounced methane growth observed over Korea during 2020–2021 was part of a broader East Asian and global atmospheric enhance-

ment, although its magnitude varied among monitoring locations, reflecting regional and site-dependent influences. Recent process-based simulations by Gaubert et al. [42] indicate that OH variability was not the dominant driver of the global CH_4 growth surge during 2020–2022, highlighting the importance of methane emissions and atmospheric transport in explaining observed CH_4 variability. Evidence from isotopic and atmospheric studies points to important contributions from microbial sources, including wetlands, agriculture, and waste, while changes in the OH sink have also been implicated [8,43–45]. The Korean observations are consistent with this broader perturbation but cannot independently resolve its global source or sink attribution. Rather, they demonstrate that the exceptional 2020–2022 methane-growth episode was expressed coherently across the Korean network while being strongly amplified by regional source and transport conditions, particularly at AMY. The seasonal pattern shown in Figure 4 provides additional evidence that this interannual perturbation was not expressed uniformly throughout the year, with relatively large departures from the annual mean growth level occurring during some summer months. This distinction provides an important context for interpreting the subsequent post-2021 deceleration in CH_4 growth, examined in Section 3.4.

3.3. Assessment of ENSO and Biomass-Burning Influences on Interannual CH_4 Variability

Large-scale climate and fire indicators provided limited evidence for a dominant control. Although several high-growth episodes coincided with La Niña conditions, consistent with the potential influence of ENSO-related temperature and precipitation anomalies on methane sources [8,35,46], Pearson correlation analysis showed no statistically significant relationships between CH_4 growth and ENSO variability at AMY ($R = 0.28$, $p = 0.27$), GSN ($R = -0.26$, $p = 0.42$), or ULD ($R = -0.41$, $p = 0.36$) (Figure 6). Similarly, correlations with biomass-burning anomalies from BOAS were $R = 0.38$ ($p = 0.14$), 0.27 ($p = 0.46$), and 0.41 ($p = 0.42$), and those with SEAS were $R = 0.26$ ($p = 0.33$), 0.07 ($p = 0.84$), and -0.24 ($p = 0.64$) for AMY, GSN, and ULD, respectively. These results indicate no statistically significant or consistent linear relationship between Korean CH_4 growth [34] and ENSO or biomass-burning variability during the analyzed periods. Individual fires may nevertheless affect the Korean individual fires may affect the Korean atmosphere under favorable transport conditions [47].

3.4. STILT-Based Transport and Regional Source Sensitivity

The observed CH_4 growth rates weakened during the recent period recent at all three monitoring stations, although the magnitude and statistical strength of the trends differed among sites. To assess the robustness of these trends while accounting for temporal autocorrelation, we additionally applied generalized least-squares (GLS) regression with ARMA error structures. The GLS analysis confirmed statistically significant negative trends at AMY and GSN. At AMY, the estimated trend was -4.63 ppb yr^{-2} (95% CI: -8.59 to -0.67; $p = 0.023$), while GSN exhibited a decrease of -3.55 ppb yr^{-2} (95% CI: -5.92 to -1.18; $p = 0.004$). At ULD, the estimated trend was also negative (-2.03 ppb yr^{-2}), but it was not statistically significant (95% CI: -4.83 to 0.76; $p = 0.151$). Thus, the recent deceleration was statistically supported at AMY and GSN, whereas the negative trend at ULD remained inconclusive.

The post-2021 deceleration is evident in both the annual time series and period-averaged growth rates (Table 1). Mean growth fell from 17.33, 15.0, and 15.7 ppb yr^{-1} at AMY, GSN, and ULD during 2019–2021 to 5.75, 7.0, and 9.0 ppb yr^{-1} during 2022–2025—declines of 67%, 53%, and 43%, respectively—compared with a 36% decline in the NOAA global record (14.04 to 8.63 ppb yr^{-1}) [48]. The stronger reductions at the Korean stations, particularly AMY, suggest that regional influences may have amplified the broader

global deceleration. This pattern is also reflected in the 2021–2025 trends in annual growth rates (Figure 4). Ordinary least-squares (OLS) regression showed significant decreases in East Asian XCH_4 (-2.04 ppb yr^{-2}, $p = 0.004$), the global record (-3.13 ppb yr^{-2}, $p = 0.002$), and GSN (-3.7 ppb yr^{-2}, $p = 0.04$), with consistent but statistically non-significant declines at AMY (-4.9 ppb yr^{-2}, $p = 0.07$) and ULD (-2.0 ppb yr^{-2}, $p = 0.20$). Although the five-year record limits statistical power, leave-one-year-out sensitivity tests consistently produced negative slopes across the surface and satellite records, supporting the robustness of the direction of the observed trends.

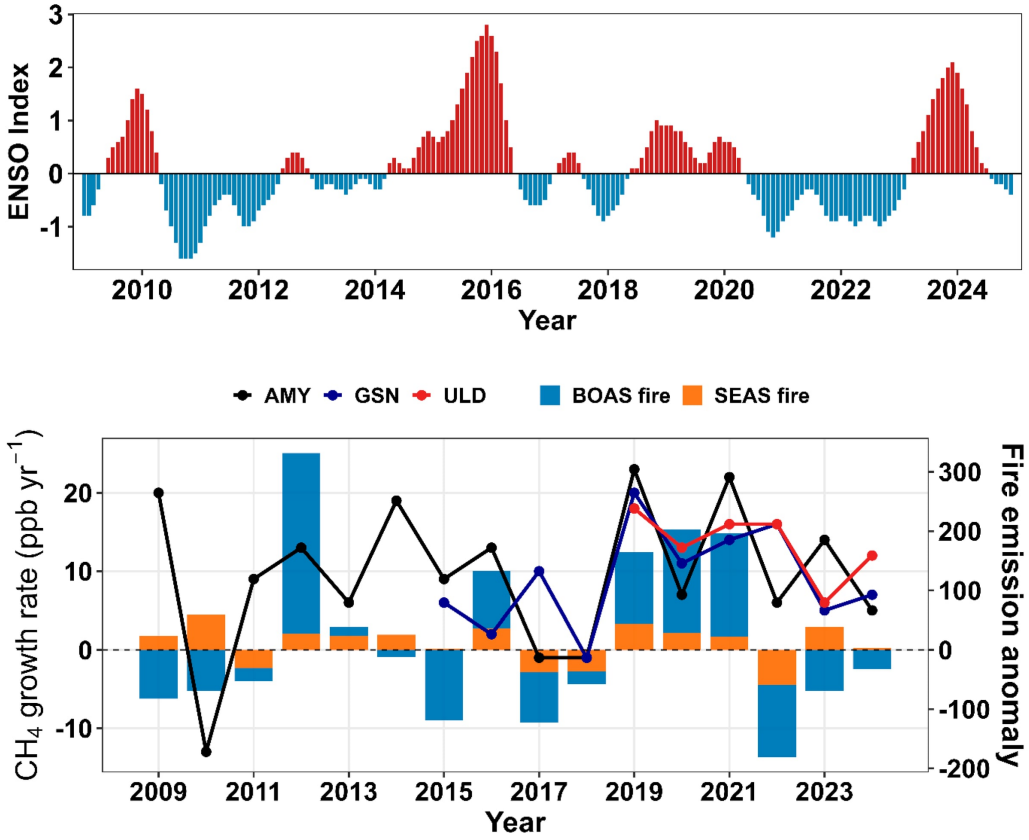

Figure 6. Large-scale climate variability, biomass-burning anomalies, and atmospheric CH_4 growth derived from in-situ stations over Korea. The upper panel shows the temporal evolution of ENSO indices and bottom panel depicts Korean atmospheric CH_4 growth rates together with fire-emission anomalies (Tonnes CH_4 yr^{-1}) during 2009–2024. BOAS—Boreal Asia covering Siberia and northern Russia; SEAS—Southeast Asia.

Table 1. Comparisons of the averaged CH_4 growth rate at Korean in-situ monitoring sites and the global average derived from NOAA global surface monitoring stations.

Time Period	The Averaged CH_4 Growth Rate (ppb yr^{-1})			
	AMY	GSN	ULD	NOAA Global Surface
2010–2018	6.0	-	-	7.35
2015–2018		4.25		
2019–2021	17.33	15.0	15.70	14.04
2022–2025	5.75	7.0	9.0	8.63

The annual mean STILT footprint distributions provide spatial context for the strong transport sensitivity identified during 2021 and subsequent years (Figure 7). The 2021 annual mean footprint was used as the reference distribution to evaluate interannual changes in AMY's sensitivity to upwind surface emissions. Accordingly, footprint ratios greater than

unity indicate enhanced sensitivity relative to 2021, whereas ratios below unity indicate reduced sensitivity. Relative to this reference, the 2022–2024 distributions show substantial spatial heterogeneity across East Asia, with both enhanced and weakened sensitivities in different source regions. In 2022, enhanced sensitivity occurred over parts of northeastern China and the northern domain, as well as portions of the southern East Asian region, while reduced sensitivity extended across substantial areas west and southwest of the Korean Peninsula. In 2023, enhanced sensitivity shifted toward parts of eastern China and the southern maritime region, whereas reduced sensitivity appeared over parts of the northwestern domain and around Japan. The 2024 distribution shared some features with 2022, including enhanced sensitivity over parts of northeastern China and the southern domain, although extensive areas of reduced sensitivity remained. These spatial contrasts indicate that the relative influence of individual upwind regions on AMY varied considerably from year to year. In particular, the footprint ratios show that the transport sensitivity associated with the 2021 reference configuration was not spatially maintained in subsequent years; instead, the geographical distribution of receptor sensitivity changed substantially. Consequently, even without equivalent changes in regional emissions, interannual variations in atmospheric transport could alter the contribution of different source regions to the CH_4 enhancement observed at AMY. This spatial evidence provides an important complement to the three-case STILT–EDGAR2025 analysis, which independently identifies a substantially stronger sensitivity of the 2021 modeled AMY enhancement to transport variability than to changes in prescribed emissions. An additional uncertainty assessment was conducted using paired moving-block bootstrap resampling and Monte Carlo simulations incorporating prescribed EDGAR emission uncertainties. Transport-related sensitivity estimates were generally larger than emission-related estimates; however, the 95% uncertainty intervals of their differences included zero, indicating that the difference was not statistically significant. These results suggest a larger modeled response to transport variability than to prescribed emission variability in AMY CH_4 enhancements, while the counterfactual experiments provide a quantitative assessment of the sensitivity of modeled receptor-level enhancements to both factors. Although these results help explain their potential roles in interannual CH_4 variability, they do not establish their exact quantitative contributions to the observed atmospheric changes. To quantify the relative sensitivity of modeled AMY enhancements to atmospheric transport and prescribed emissions, we conducted a three-case STILT–EDGAR2025 counterfactual analysis (Figure 8). Relative to the 2018 baseline, the transport-only simulation (Case 2) closely followed the fully varying simulation (Case 1) during 2019–2024, whereas the emission-only simulation (Case 3) exhibited substantially smaller interannual variability. The 2021 CH_4 enhancement anomaly was 22.0 ppb, of which the transport- and emission-sensitive anomalies were 18.4 and 3.4 ppb, respectively. This contrast indicates that the exceptional 2021 modeled enhancement was substantially more sensitive to changes in source–receptor transport pathways than to changes in the prescribed emission field. This interpretation was qualitatively unchanged when 2019 was used as the reference year, even though the magnitudes of the sensitivity metrics depend on the selected reference state. After 2021, transport sensitivity also exceeded emission sensitivity, although its magnitude varied considerably among years. The transport- and emission-sensitive anomalies were 4.1 and 2.4 ppb in 2022, 11.7 and 1.0 ppb in 2023, and 2.1 and 0.7 ppb in 2024, respectively. The pronounced transport-sensitive increase in 2023 illustrates how interannual changes in atmospheric circulation can temporarily amplify receptor-level CH_4 enhancements, even when changes in the prescribed emissions contribute relatively little. The counterfactual anomalies are sensitivity metrics rather than an additive decomposition of the total CH_4 anomaly because receptor enhancements depend jointly on transport and emissions. The analysis also identifies Korea as the dominant source region of the mod-

eled AMY enhancement under the prescribed configuration. Overall, the footprint and counterfactual analyses consistently demonstrate that atmospheric transport was a major modulator of interannual CH_4 enhancement variability at AMY, while regional emissions provided an important source contribution.

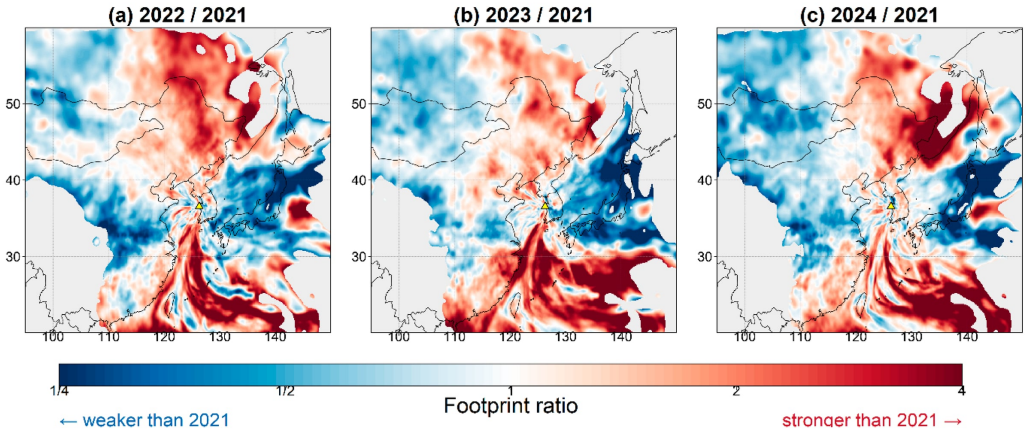

Figure 7. Spatial distribution of annual mean STILT footprint ratios at AMY for 2022, 2023, and 2024 relative to the 2021 reference year. Ratios greater than 1 indicate enhanced sensitivity of the AMY receptor to upwind surface emissions compared with 2021, whereas ratios below 1 indicate reduced sensitivity.



Figure 8. Three-case counterfactual analysis of CH_4 enhancement (ΔCH_4) at Anmyeondo (AMY), 2019–2024. (**a**) Annual enhancements under actual transport and emissions (Case 1); Case 2: representing sensitivity to variable transport under fixed 2018 emissions); and Case 3: representing sensitivity to variable emissions under fixed 2018 transport, shown separately for East Asia (total) and Korea. (**b**) Corresponding anomalies relative to the 2018 baseline for the same three cases. Enhancements were calculated from STILT footprint–EDGAR2025 monthly emission products.

3.5. Post-2021 CH_4 Growth-Rate Deceleration: Integrated Interpretation of Transport and Regional Emissions

The EDGAR2025 inventory provides complementary evidence for changes in regional emission tendencies (Figure 9). China remained the dominant anthropogenic source, with only a weak decreasing tendency (-0.062 Tg CH_4 yr^{-2}, $p = 0.61$) and heterogeneous sectoral behavior—agriculture, fuel exploitation, power, and waste generally weakened, whereas buildings and several industrial sectors increased. However, the year-to-year changes reveal substantial interannual variability, particularly in fuel exploitation and agriculture. Fuel exploitation showed substantial positive contributions in 2021 and 2023, contrasting with negative changes in fuel exploitation and agriculture in 2022 and 2024. Korea showed a stronger but only marginally significant decline in total emission growth (-0.033 Tg CH_4 yr^{-2}, $p = 0.078$), driven mainly by agriculture (-0.0092 Tg CH_4 yr^{-2}, $p = 0.06$) and waste (-0.0248 Tg CH_4 yr^{-2}, $p = 0.15$); the significant increase in buildings ($+0.00029$ Tg CH_4 yr^{-2}, $p = 0.03$) was too small to alter the overall tendency. At the annual scale, positive emission changes in 2020 and 2021 were largely associated with the waste sector, whereas total annual changes became negative in 2023 and 2024. The 2023 decrease was primarily associated with waste emissions, while the 2024 decrease was mainly driven by agricultural emissions. Overall, EDGAR2025 indicates weakening Korean emission growth after 2021, but with sectorally heterogeneous changes. Given the short 2020–2024 period, these slopes are interpreted as descriptive indicators of recent emission tendencies rather than robust long-term trends.

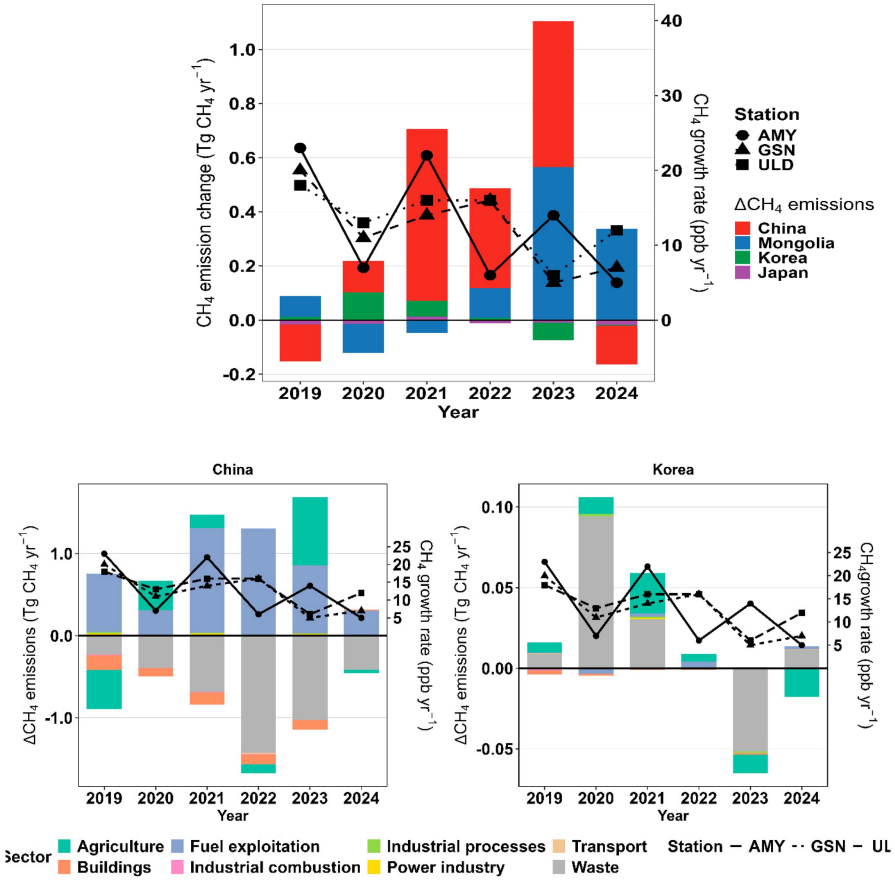

Figure 9. Country-level and sectoral changes in anthropogenic CH_4 emissions across major East Asian countries and their temporal relationship with atmospheric CH_4 growth at the AMY, GSN, and ULD stations during 2020–2024. Country-level emission changes are shown together with the contributions from individual anthropogenic sectors.

Taken together, the observations, STILT–EDGAR2025 counterfactuals, and EDGAR2025 inventory provide complementary evidence that the post-2021 slowdown in atmospheric CH_4 growth occurred alongside weaker regional emission growth, while interannual transport variability strongly modulated the magnitude of the signal observed at AMY. Atmospheric CH_4 variability over Korea therefore reflects the combined influence of regional source changes and atmospheric transport, with background conditions and atmospheric removal remaining unresolved. Uncertainties in EDGAR2025 emissions, background concentrations, boundary conditions, and OH variability limit quantitative attribution; accordingly, the STILT–EDGAR results should be interpreted as receptor-scale sensitivities rather than a complete CH_4 source–sink budget. Recent studies have also linked part of the global CH_4 growth-rate deceleration to changes in atmospheric OH [8,9,43–45,49], but because OH was not measured or explicitly simulated here, its contribution to the Korean slowdown cannot be quantified.

4. Conclusions

Understanding the drivers of recent changes in atmospheric CH_4 growth over East Asia is essential for interpreting the global methane surge and assessing regional emission variability. This study provides a network-wide assessment of atmospheric CH_4 variability over the Korean Peninsula using observations from the AMY (2009–2025), GSN (2014–2025), and ULD (2015–2025) GAW stations, complemented by satellite XCH_4 observations, emission inventories, and receptor-scale transport analysis. By combining observations from stations with contrasting source-region and transport sensitivities, this study identifies both coherent regional changes and substantial site-specific variability in atmospheric CH_4. The analysis of the complete historical records (2009–2025) places the recent weakening of methane growth rates within a broader transition around 2021–2022. This transition was most clearly supported by the global and East Asian satellite records.

The most prominent interannual feature was the strong CH_4 growth during 2020–2022, followed by pronounced deceleration after 2021. During 2019–2021, mean growth rates reached 17.3, 15.0, and 15.7 ppb yr^{-1} at AMY, GSN, and ULD, respectively, before decreasing substantially during 2022–2025. The larger reductions at the Korean stations than in the global record, together with coherent variability among the three stations and agreement with East Asian and global satellite XCH_4 observations, indicate that the recent deceleration reflects broader atmospheric changes accompanied by regional modulation. The particularly strong response at AMY highlights the sensitivity of coastal Korea to variations in regional source–receptor relationships. A further important finding was the pronounced increase in seasonal CH_4 amplitude at AMY, from 67.1 ppb in 2022 to 119.2 ppb in 2025 (approximately 78%). This widening reflected changes in both the seasonal maximum and minimum: the initial increase was dominated by rising maxima, while the subsequent expansion was increasingly reinforced by lower summer minima. Because seasonal amplitude integrates the effects of emissions, atmospheric transport, and removal, the observed increase cannot be uniquely attributed to a single process. Nevertheless, it indicates a substantial recent change in the seasonal structure of atmospheric CH_4 variability at AMY.

The STILT–EDGAR2025 counterfactual experiments provide additional insight into the processes influencing receptor-level CH_4 enhancements. Relative to the 2018 reference configuration, the modeled AMY enhancement in 2021 exhibited substantially greater sensitivity to transport variability (18.4 ppb) than to changes in prescribed emissions (3.4 ppb). These values represent sensitivity metrics rather than a quantitative partition of the observed atmospheric CH_4 anomaly. The experiments also identify Korea as a major contributor to the modeled AMY enhancement under the prescribed configuration. Meanwhile, EDGAR2025 indicates a weakening in the rate of regional year-to-year emission growth

after the early-2020s acceleration, particularly over Korea, although the magnitude and statistical significance vary among sectors and regions. Together, these findings demonstrate that changes in regional emissions and atmospheric transport both matter for interpreting observed CH_4 variability, while transport can exert a particularly strong influence on the enhancement measured at an individual receptor. Importantly, a slowdown in emission growth does not necessarily indicate a decline in absolute emissions.

Overall, the combined surface, satellite, inventory, and transport analyses show that the post-2021 weakening of atmospheric CH_4 growth over Korea occurred alongside substantial changes in regional source conditions and receptor-level transport sensitivity. The Korean GAW network therefore provides an important regional constraint on methane variability in East Asia and demonstrates the limitations of interpreting atmospheric CH_4 changes from emission trends alone. Nevertheless, this study does not provide a closed methane budget or quantitatively separate the effects of regional emissions, atmospheric transport, and chemical removal. In particular, changes in atmospheric OH oxidation were not directly evaluated and remain an unresolved potential contributor. Future studies integrating time-varying atmospheric inversions, satellite observations, improved regional emission inventories, and process-based atmospheric chemistry modeling will be essential to quantify the relative contributions of these processes and to strengthen the assessment of regional methane mitigation.

Author Contributions: S.T.K.: Conceptualization, writing—original draft, methodology, investigation, formal analysis, data curation; D.S.: review & editing, resources; W.S.: review & editing, resources; S.L.: review & editing; S.K.: review & editing, project administration; S.K.: review & editing, project administration. All authors have read and agreed to the published version of the manuscript.

Funding: This work was funded by the Korea Meteorological Administration Research and Development Program "Developing Technology for Integrated Climate Change Monitoring and Analysis" under Grant (KMA2018-00324).

Data Availability Statement: The EDGAR2025 emission inventory data are publicly available from the Emissions Database for Global Atmospheric Research (EDGAR) of the European Commission Joint Research Centre (JRC). EDGAR2025 data portal (https://edgar.jrc.ec.europa.eu/dataset_ghg2025accessed on 25 June 2026). Biomass-burning CH_4 emissions were obtained from the Global Fire Emissions Database version 5 (GFED5) https://www.globalfiredata.org/tables/GFED5.1_CH4.txt accessed on 20 May 2026). ERA5 meteorological reanalysis data are available through the Copernicus Climate Data Store (CDS) (https://cds.climate.copernicus.eu/ accessed on 1 June 2026). TROPOMI/Sentinel-5P L3 gridded XCH_4 data are available via (https://browser.moregeo.it/external/data-portal.s5p-pal.com/api/s5p-l3/ch4/ accessed on 10 July 2026). GOSAT XCH_4 data are available from the GOSAT Data Archive Service (GDAS) (https://data2.gosat.nies.go.jp accessed on 15 May 2026) operated by the National Institute for Environmental Studies (NIES). The in-situ CH_4 mole fractions data (Anmyeondo, Gosan, and Ulleungdo sites) are available from World Data Centre for Greenhouse Gases (WDCGG) (https://gaw.kishou.go.jp).

Conflicts of Interest: The authors declare no conflicts of interest.

Abbreviations

The following abbreviations are used in this manuscript:

AMY	Anmyeondo
GSN	Gosan
ULD	Ulleungdo
CH_4	Methane
XCH_4	Column-averaged dry-air mole fraction of methane
EDGAR 2025	Emissions Database for Global Atmospheric Research, 2025 version
ENSO	El Niño–Southern Oscillation

GAW	Global Atmosphere Watch
GML	Global Monitoring Laboratory
GOSAT	Greenhouse Gases Observing Satellite
NOAA	National Oceanic and Atmospheric Administration
OH	Hydroxyl radical
STILT	Stochastic Time-Inverted Lagrangian Transport
TROPOMI	TROPOspheric Monitoring Instrument
WMO	World Meteorological Organization
ECMWF	European Centre for Medium-Range Weather Forecasts
ERA5	fifth-generation ECMWF reanalysis produced by the Copernicus Climate Change Service (C3S)

References

1. Prather, M.J.; Holmes, C.D.; Hsu, J. Reactive greenhouse gas scenarios: Systematic exploration of uncertainties and the role of atmospheric chemistry. *Geophys. Res. Lett.* **2012**, *39*, L09803. [CrossRef]
2. Etminan, M.; Myhre, G.; Highwood, E.J.; Shine, K.P. Radiative forcing of carbon dioxide, methane, and nitrous oxide: A significant revision of the methane radiative forcing. *Geophys. Res. Lett.* **2016**, *43*, 12614–12623. [CrossRef]
3. Forster, P.; Storelvmo, T.; Armour, K.; Collins, W.; Dufresne, J.-L.; Frame, D.; Lunt, D.J.; Mauritsen, T.; Palmer, M.D.; Watanabe, M.; et al. The Earth's energy budget, climate feedbacks, and climate sensitivity. In *Climate Change 2021: The Physical Science Basis*; Contribution of Working Group I to the Sixth Assessment Report of the Intergovernmental Panel on Climate Change; Cambridge University Press: Cambridge, UK, 2021; pp. 923–1054. [CrossRef]
4. United Nations Environment Programme; Climate and Clean Air Coalition (UNEP/CCAC). *Global Methane Assessment: Benefits and Costs of Mitigating Methane Emissions*; United Nations Environment Programme: Nairobi, Kenya, 2021.
5. International Energy Agency (IEA). *Global Methane Pledge—Policies*; International Energy Agency: Paris, France, 2021. Available online: https://www.iea.org/policies/14257-global-methane-pledge (accessed on 3 August 2026).
6. Nisbet, E.G.; Manning, M.R.; Dlugokencky, E.J.; Fisher, R.E.; Lowry, D.; Michel, S.E.; Myhre, C.L.; Platt, S.M.; Allen, G.; Bousquet, P.; et al. Very strong atmospheric methane growth in the four years 2014–2017: Implications for the Paris Agreement. *Glob. Biogeochem. Cycles* **2019**, *33*, 318–342. [CrossRef]
7. Saunois, M.; Martinez, A.; Poulter, B.; Zhang, Z.; Raymond, P.A.; Regnier, P.; Canadell, J.G.; Jackson, R.B.; Patra, P.K.; Bousquet, P.; et al. Global Methane Budget 2000–2020. *Earth Syst. Sci. Data* **2025**, *17*, 1873–1958. [CrossRef]
8. Peng, S.; Lin, X.; Thompson, R.L.; Xi, Y.; Liu, G.; Hauglustaine, D.; Lan, X.; Poulter, B.; Ramonet, M.; Saunois, M.; et al. Wetland emission and atmospheric sink changes explain methane growth in 2020. *Nature* **2022**, *612*, 477–482. [CrossRef] [PubMed]
9. He, M.; Jacob, D.J.; Estrada, L.A.; Varon, D.J.; Sulprizio, M.; Balasus, N.; East, J.D.; Penn, E.; Pendergrass, D.C.; Chen, Z.; et al. Attributing 2019–2024 methane growth using TROPOMI satellite observations. *Sci. Adv.* **2026**, *12*, eadz9007. [CrossRef] [PubMed]
10. Hu, H.; Landgraf, J.; Detmers, R.; Borsdorff, T.; Aan de Brugh, J.; Aben, I.; Butz, A.; Hasekamp, O. Toward global mapping of methane with TROPOMI: First results and intersatellite comparison to GOSAT. *Geophys. Res. Lett.* **2018**, *45*, 3682–3689. [CrossRef]
11. Qu, Z.; Jacob, D.J.; Shen, L.; Lu, X.; Zhang, Y.; Scarpelli, T.R.; Nesser, H.; Sulprizio, M.P.; Maasakkers, J.D.; Bloom, A.A.; et al. Global distribution of methane emissions: A comparative inverse analysis of observations from the TROPOMI and GOSAT satellite instruments. *Atmos. Chem. Phys.* **2021**, *21*, 14159–14175. [CrossRef]
12. Chen, Z.; Jacob, D.J.; Nesser, H.; Sulprizio, M.P.; Lorente, A.; Varon, D.J.; Lu, X.; Shen, L.; Qu, Z.; Penn, E.; et al. Methane emissions from China: A high-resolution inversion of TROPOMI satellite observations. *Atmos. Chem. Phys.* **2022**, *22*, 10809–10826. [CrossRef]
13. Lee, H.; Seo, W.; Li, S.; Lee, S.; Kenea, S.T.; Joo, S. Measurement report: Atmospheric CH_4 at regional stations of the Korea Meteorological Administration–Global Atmosphere Watch Programme: Measurement, characteristics, and long-term changes of its drivers. *Atmos. Chem. Phys.* **2023**, *23*, 7141–7159. [CrossRef]
14. Kenea, S.T.; Lee, H.Y.; Joo, S.W.; Li, S.L.; Labzovskii, L.D.; Chung, C.Y.; Kim, Y.H. Interannual variability of atmospheric CH_4 and its driver over South Korea captured by integrated data in 2019. *Remote Sens.* **2021**, *13*, 2266. [CrossRef]
15. Geum, S.; Park, H.; Choi, H.; Kim, Y.; Lee, H.; Joo, S.; Oh, Y.-S.; Michel, S.E.; Park, S. Identifying emission sources of CH_4 in East Asia based on in-situ observations of atmospheric 13C-CH_4 and C_2H_6. *Sci. Total Environ.* **2024**, *908*, 168433. [CrossRef] [PubMed]
16. Kenea, S.T.; Shin, D.; Lee, S.; Wang, F.; Maksyutov, S.; Joo, S.; Lee, S.; Kim, S. Methane (CH_4) emission estimates for South Korea using Lagrangian-based inversion modeling (2010–2021). *Atmos. Environ. X* **2026**, *30*, 100440. [CrossRef]
17. Shin, H.Y.; Kim, J.; Shin, D.; Kim, S.; Lee, S.; Lee, Y.G. Spatiotemporal Variability of Greenhouse Gas Concentrations at the WMO/GAW Observational Sites in Korea. *Atmosphere* **2025**, *16*, 1352. [CrossRef]
18. Pinheiro, J.C.; Bates, D.M. *Mixed-Effects Models in S and S-PLUS*; Springer: New York, NY, USA, 2000. [CrossRef]

19. Box, G.E.P.; Jenkins, G.M.; Reinsel, G.C.; Ljung, G.M. *Time Series Analysis: Forecasting and Control*, 5th ed.; Wiley: Hoboken, NJ, USA, 2016.
20. Ljung, G.M.; Box, G.E.P. On a measure of lack of fit in time series models. *Biometrika* **1978**, *65*, 297–303. [CrossRef]
21. Breusch, T.S.; Pagan, A.R. A simple test for heteroscedasticity and random coefficient variation. *Econometrica* **1979**, *47*, 1287–1294. [CrossRef]
22. Engle, R.F. Autoregressive conditional heteroscedasticity with estimates of the variance of United Kingdom inflation. *Econometrica* **1982**, *50*, 987–1007. [CrossRef]
23. Lin, J.C.; Gerbig, C.; Wofsy, S.C.; Daube, B.C.; Matross, D.M.; Chow, V.Y.; Gottlieb, E.W.; Kofler, J.; Holloway, J.S.; Hsueh, D.Y.; et al. A near-field tool for simulating the upstream influence of atmospheric observations: The Stochastic Time-Inverted Lagrangian Transport (STILT) model. *J. Geophys. Res. Atmos.* **2003**, *108*, 4493. [CrossRef]
24. Gerbig, C.; Lin, J.C.; Wofsy, S.C.; Daube, B.C.; Andrews, A.E.; Stephens, B.B.; Bakwin, P.S.; Grainger, C.A. Toward constraining regional-scale fluxes of CO_2 with atmospheric observations over a continental scale. *J. Geophys. Res. Atmos.* **2003**, *108*, 4756. [CrossRef]
25. Hersbach, H.; Bell, B.; Berrisford, P.; Hirahara, S.; Horányi, A.; Muñoz-Sabater, J.; Nicolas, J.; Peubey, C.; Radu, R.; Schepers, D.; et al. The ERA5 global reanalysis. *Q. J. R. Meteorol. Soc.* **2020**, *146*, 1999–2049. [CrossRef]
26. Morino, I.; Uchino, O.; Inoue, G.; Yoshida, Y.; Yokota, T.; Suto, H.; Tanimoto, H.; Ganshin, A.; Matsueda, H.; Sawa, Y.; et al. Preliminary validation of column-averaged volume mixing ratios of carbon dioxide and methane retrieved from GOSAT short-wavelength infrared spectra. *Atmos. Meas. Tech.* **2011**, *4*, 1061–1076. [CrossRef]
27. Yoshida, Y.; Ota, Y.; Eguchi, N.; Kikuchi, N.; Kuze, A.; Suto, H.; Nakajima, T.; Yokota, T. Retrieval algorithm for CO_2 and CH_4 column abundances from short-wavelength infrared spectral observations by the Greenhouse Gases Observing Satellite. *Atmos. Meas. Tech.* **2011**, *4*, 717–734. [CrossRef]
28. Yoshida, Y.; Kikuchi, N.; Morino, I.; Uchino, O.; Suto, H.; Schneising, O.; Bönisch, H.; Blume, N.; Lindauer, M.; Kaiser, J.W.; et al. Improvement of the retrieval algorithm for GOSAT SWIR XCO_2 and XCH_4 and their validation using TCCON data. *Atmos. Meas. Tech.* **2013**, *6*, 1533–1547. [CrossRef]
29. Hu, H.; Hasekamp, O.; Butz, A.; Galli, A.; Landgraf, J.; Aan de Brugh, J.; Borsdorff, T.; Scheepmaker, R.; Aben, I. The Operational Methane Retrieval Algorithm for TROPOMI. *Atmos. Meas. Tech.* **2016**, *9*, 5423–5440. [CrossRef]
30. Lorente, A.; Borsdorff, T.; Butz, A.; Hasekamp, O.; Aan de Brugh, J.; Schneider, A.; Wu, L.; Hase, F.; Borchardt, J.; Landgraf, J. Methane retrieved from TROPOMI: Improvement of the data product and validation of the first 2 years. *Atmos. Meas. Tech.* **2021**, *14*, 665–684. [CrossRef]
31. Sha, M.K.; Lunt, M.F.; Commane, R.; Hase, F.; Kivi, R.; Lindauer, M.; Philippon, C.; Ramonet, M.; Scheeren, B.; Shaffrey, L.; et al. Validation of methane satellite retrievals from TROPOMI onboard Sentinel-5 Precursor using TCCON and NDACC-IRWG networks. *Atmos. Meas. Tech.* **2021**, *14*, 6245–6274. [CrossRef]
32. Crippa, M.; Guizzardi, D.; Pagani, F.; Schiavina, M.; Melchiorri, M.; Pisoni, E.; Graziosi, F.; Muntean, M.; Maes, J.; Dijkstra, L.; et al. Insights into the Spatial Distribution of Global, National, and Subnational Greenhouse Gas Emissions in the Emissions Database for Global Atmospheric Research (EDGAR v8.0). *Earth Syst. Sci. Data* **2024**, *16*, 2811–2830. [CrossRef]
33. Crippa, M.; Guizzardi, D.; Pagani, F.; Banja, M.; Muntean, M.; Quadrelli, R.; Risquez Martin, A.; Taghavi-Moharamli, P.; Köykkä, J.; Grassi, G.; et al. *GHG Emissions of All World Countries—2025 Report*; JRC143227; Publications Office of the European Union: Luxembourg, 2025. [CrossRef]
34. van der Werf, G.R.; Randerson, J.T.; van Wees, D.; Chen, Y.; Giglio, L.; Hall, J.; Vernooij, R.; Mu, M.; Shahid, S.B.; Barsanti, K.C.; et al. Landscape Fire Emissions from the 5th Version of the Global Fire Emissions Database (GFED5). *Sci. Data* **2025**, *12*, 1870. [CrossRef] [PubMed]
35. Trenberth, K.E.; Hoar, T.J. El Niño and climate change. *J. Geophys. Res. Lett.* **1997**, *24*, 3057–3060. [CrossRef]
36. Dlugokencky, E.J.; Steele, L.P.; Lang, P.M.; Masarie, K.A. Atmospheric methane at Mauna Loa and Barrow observatories: Presentation and analysis of in situ measurements. *J. Geophys. Res. Atmos.* **1995**, *100*, 23103–23113. [CrossRef]
37. Tran, D.A.; Vilà-Guerau de Arellano, J.; Luijkx, I.T.; Gerbig, C.; Gałkowski, M.; Botía, S.; Faassen, K.; Zaehle, S. Increasing diurnal and seasonal amplitude of atmospheric methane mole fraction in Central Siberia between 2010–2021. *Atmos. Chem. Phys.* **2025**, *25*, 16553–16588. [CrossRef]
38. Liu, G.; Shen, L.; Ciais, P.; Lin, X.; Hauglustaine, D.; Lan, X.; Turner, A.J.; Xi, Y.; Zhu, Y.; Peng, S. Trends in the seasonal amplitude of atmospheric methane. *Nature* **2025**, *641*, 660–665. [CrossRef] [PubMed]
39. Michel, S.E.; Lan, X.; Miller, J.; Tans, P.; Clark, J.R.; Schaefer, H.; Sperlich, P.; Brailsford, G.; Morimoto, S.; Moossen, H.; et al. Rapid shift in methane carbon isotopes suggests microbial emissions drove record high atmospheric methane growth in 2020–2022. *Proc. Natl. Acad. Sci. USA* **2024**, *121*, e2411212121. [CrossRef] [PubMed]
40. Li, S.; Kim, Y.; Kim, J.; Kenea, S.T.; Goo, T.-Y.; Labzovskii, L.D.; Byun, Y.-H. In situ aircraft measurements of CO_2 and CH_4: Mapping spatio-temporal variations over western Korea in high-resolutions. *Remote Sens.* **2020**, *12*, 3093. [CrossRef]

41. Japan Meteorological Agency (JMA). *Climate Change Monitoring Report 2022*; Japan Meteorological Agency: Tokyo, Japan, 2022. Available online: https://www.jma.go.jp/jma/en/NMHS/ccmr/ccmr2022.pdf (accessed on 7 November 2026).
42. Gaubert, B.; Mirrezaei, M.A.; Fernandez, R.P.; Ortega, I.; Emmons, L.; Orlando, J.; Oh, Y.; Bruhwiler, L.; Chen, S.; Pétron, G.; et al. Tropospheric oxidation chemistry and methane growth: A process-based attribution of OH variability (2003–2022). *Atmos. Chem. Phys.* **2026**, *26*, 15683–15719. [CrossRef]
43. Qu, Z.; Jacob, D.J.; Zhang, Y.; Shen, L.; Varon, D.J.; Lu, X.; Scarpelli, T.; Bloom, A.; Worden, J.; Parker, R.J. Attribution of the 2020 surge in atmospheric methane by inverse analysis of GOSAT observations. *Environ. Res. Lett.* **2022**, *17*, 094003. [CrossRef]
44. Feng, L.; Palmer, P.I.; Parker, R.J.; Lunt, M.F.; Bösch, H. Methane emissions are predominantly responsible for record-breaking atmospheric methane growth rates in 2020 and 2021. *Atmos. Chem. Phys.* **2023**, *23*, 4863–4880. [CrossRef]
45. Ciais, P.; Zhu, Y.; Cai, Y.; Lan, X.; Michel, S.E.; Zheng, B.; Zhao, Y.; Hauglustaine, D.A.; Lin, X.; Zhang, Y.; et al. Why methane surged in the atmosphere during the early 2020s. *Science* **2026**, *391*, eadx8262. [CrossRef] [PubMed]
46. Bousquet, P.; Ringeval, B.; Pison, I.; Dlugokencky, E.J.; Brunke, E.-G.; Carouge, C.; Chevallier, F.; Fortems-Cheiney, A.; Frankenberg, C.; Hauglustaine, D.A.; et al. Contribution of anthropogenic and natural sources to atmospheric methane variability. *Nature* **2006**, *443*, 439–443. [CrossRef] [PubMed]
47. Worden, J.R.; Bloom, A.A.; Pandey, S.; Jiang, Z.; Worden, H.M.; Walker, T.W.; Houweling, S.; Röckmann, T. Reduced biomass burning emissions reconcile conflicting estimates of the post-2006 atmospheric methane budget. *Nat. Commun.* **2017**, *8*, 2227. [CrossRef] [PubMed]
48. Lan, X.; Thoning, K.W.; Dlugokencky, E.J. *Trends in Globally-Averaged CH_4, N_2O, and SF_6 Determined from NOAA Global Monitoring Laboratory Measurements*; Version 2026-08; Global Monitoring Laboratory: Boulder, CO, USA, 2022. [CrossRef]
49. Belikov, D.A.; Patra, P.K.; Saitoh, N. Hydroxyl interannual variability impacts estimation of regional methane emissions. *J. Geophys. Res. Atmos.* **2026**, *131*, e2025JD044457. [CrossRef]

Disclaimer/Publisher's Note: The statements, opinions and data contained in all publications are solely those of the individual author(s) and contributor(s) and not of MDPI and/or the editor(s). MDPI and/or the editor(s) disclaim responsibility for any injury to people or property resulting from any ideas, methods, instructions or products referred to in the content.